Front. Struct. Civ. Eng. 2019, 13(5): 1200–1213
https://doi.org/10.1007/s11709-019-0546-2

RESEARCH ARTICLE

The influence of hand hole on the ultimate strength and crack pattern of shield tunnel segment joints by scaled model test

Shaochun WANG, Xi JIANG, Yun BAI*

Department of Geotechnical Engineering, College of Civil Engineering, Tongji University, Shanghai 200092, China
**Corresponding author. E-mail: baiyun1958@tongji.edu.cn*

ABSTRACT With the shield tunnel going deeper and deeper, the circumferential axial force becomes the governing factor rather than the bending moment. The hand hole acts as a weak point and initial damage in the segment joint especially when the circumferential axial force is extremely high. Despite the wide application of steel fiber or synthetic fiber in the tunneling, limited researches focus on the structural responses of segment joint with macro structural synthetic fiber (MSSF). In this paper, a 1:2 reduced-scale experiment was conducted to study the structural performance of the segment joint with different types of hand holes under ultra-high axial force. Special attention is paid to failure mode and structural performance (bearing capacity, deformation, cracking, and toughness). Moreover, segment joints with MSSF are also tested to evaluate the effects of MSSF on the failure mode and structural performance of the segment joints. The experiment results show that the hand hole becomes the weakest point of the segment joint under ultra-high axial force. A \ /-type crack pattern is always observed before the final failure of the segment joints. Different types and sizes of the hand hole have different degree of influences on the structural behavior of segment joints. The segment joint with MSSF shows higher ultimate bearing capacity and toughness compared to segment joint with common concrete. Besides, the MSSF improves the initial cracking load and anti-spallling resistance of the segment joint.

KEYWORDS shield tunneling, structural synthetic fiber concrete, hand hole, segment joint, ultimate bearing capacity, crack pattern

1 Introduction

In recent decades, the use of deep underground space beneath seas and rivers became an alternative solution to urban land resources. Many new tunnel utilities including undersea and riverbed tunnels in China have been constructed at progressively greater depths by shield tunneling method, such as the Qiongzhou Strait Tunnel. For such undersea tunnels, it is important to account for hydrostatic pressures acting as additional load on the operating shield tunnel [1,2]. Under ultra-high water pressure, the tunnel lining are governed by the circular axial force rather than the bending moment. Therefore, the axial force acting on the cross section plays a leading role in the design of segment lining. To ensure the ultimate bearing capacity, the increase in the thickness of segment lining inevitably causes uneconomically and inconveniently construction. Under this circumstance, the loss of effective area and stress concentrations caused by the hand hole, which is usually neglected in general underwater tunnels, should be considered because of the potential damage to ultimate bearing capacity with limited thickness of segments.

Previous research mostly focused on the structural response of such tunnel segments subjected to both positive and negative bending moments under constant axial force states. The biaxial loading is often simplified as uniaxial loading since the bending moment is neglected under ultra-high water pressure. Moreover, previous researches focused on the main segment rather than the segment joints. However, the segmental joints are the most vulnerable points in the entire tunnel structure as the joints exhibit a considerably smaller bearing capacity than the main segments [3–6]. Through experimental tests Feng

Article history: Received Jul 29, 2018; Accepted Oct 7, 2018

et al. [7] and Liu et al. [8] have shown that the failure of the segment lining originates from the joint. To improve future tunnel structures, it is essential to gain a better understanding on the structural response and failure mechanism of the segment joint with hand hole under ultra-high water pressure. Besides experimental testing, which will be pursued in this manuscript, computational modeling can be exploited. Computational modeling provides the opportunity to extract phenomena which are difficult to assess experimentally [9–12], for instance to study the interaction between the reinforcement and the matrix material [13]. Commonly structural element formulations are exploited [14–16] which can be applied to larger structures. The immersed particle method from Rabczuk et al. [17] is also capable of accounting for the interaction between the fluid and the structure in the case of failure. However, such formulations are not well suited to cover complex failure mechanisms as they occur locally in tunnel structures. For these purposes, continuum approaches to fracture are more common. Efficient remeshing techniques [18–24], cracking particle methods [25–27], enriched methods [28–30], peridynamics and dual-horizon peridynamics [31,32], as well as certain meshfree methods [33] belong to the most popular discrete approaches to fracture while phase field models [34,35] or models based on the screened-Poisson equations [18,20] belong to common continuous approaches to fracture. An interesting contribution accounting for the hydro-mechanical nature has been proposed for instance by Zhuang et al. [36].

Fiber reinforced concrete has been gradually adopted as a solution to improve the structural behavior of segment lining in terms bearing capacity, cracking resistance, and toughness. Although Steel Fiber Reinforced Concrete (SFRC) has been first applied in tunneling, in the last decade, several types of MSSF have been exploited to replace SFRC. According to previous research, MSSF could not only increase the structural behavior of concrete but also guarantee the long-term performance since MSSF do not suffer from corrosion problems. With ultra-high water pressure acting on the segment lining, the thickness of the segment lining has to be enlarged to meet the requirement of ultimate bearing capacity. However, the increased tunnel size cannot avoid localized stress caused by irregularities during the tunnel construction (e.g., eccentricity of jacks, gaps between rings). Previous research showed that the fiber enables a stable development of splitting cracks, leading to relatively small cracks and a possible reduction or elimination of stirrups placed in the regions under high localized stress. Moreover, it was proved that adding fibers to concrete helps to prevent premature separation of the concrete cover. In addition, fibers help to prevent local damage as spalling at edges and chipping of corners [37].

This paper presents segment joint tests subjected to concentric axial loading. The main objective of this research is to investigate the structural performance of the segment joint with hand hole under ultra-high water pressure. Special attention is paid to the cracking process and failure mechanism. Segment joints with different types of hand holes are tested to investigate their influences on the failure mode and structural performance (bearing capacity, deformation, cracking, and toughness) of the segment joints. A detailed comparison is subsequently performed to provide suggestions for future designs of segment joints with hand hole. Moreover, segment joints with MSSF are also tested to study the effects of MSSF on the failure mode and structural performance of the segment joints. A detailed comparison is subsequently performed to highlight the potential of using MSSF in tunnel applications.

2 Experimental program

2.1 Prototype and specimen design

The 1:2 reduced-scale experimental program included 9 groups of segment joints specimens varying in the shape of hand hole and the volume fraction of MSSF. The specimen names include the type of joint (JS, JB, and JI), the shape of hand hole (Rec, stm, and tra), the volume ratio of fiber (0 and 0.55%) and the ratio of longitudinal reinforcement (0, 1.24%, and 1.93%). JS, JB, and JI are the abbreviations for Straight joint, Bending joint, and Incline joint, respectively. Rec, stm, and tra stand for rectangle, streamline, and trapezoid, respectively. The last group in Table 1, which was designed as control group without hand hole, was named COL_STD_0_1.93. To determine the dimension and corresponding details of the segment joint specimens, a survey was conducted based on several completed tunnel projects in China. Considering the ultra-high water pressure faced in Qiongzhou Strait Tunnel, the length, width, and thickness of the segment prototype is 2000 mm, 2000 mm, and 700 mm, respectively. Concerning about the symmetry, fabrication, and transportation of the segments, 1/3 width of the segment joint was cast by reduced scale of 1:2 for testing. The practical arc-shaped segment was replaced by flat-shaped segment for the convenience of fabrication and testing. Actually, this simplification has been already applied in the previous experiments. According to Saint-Venant's Principle [38], there is no need to test the whole length of the segment because the obvious structural response of the joint is limited to the end region. Figure 1 illustrates the simplicity and equivalence process in this test. Focusing on the influence of the hand hole, the joint surface is designed into smooth surface, i.e., some details of the joint characteristics (gasket groove, caulking groove, convex concrete surface and gasket) are neglected. Besides, the connection bolts are not used in the test since they are non-structural components under

Table 1 Joint component geometry details

joint	Qty.	hole shape	l (mm)	w (mm)	d	V_f	A_s (mm^2)
JS_REC_0_1.93	3	rectangle	250	80	170	0%	2260
JB_REC_0_1.93	3	rectangle	200	80	130	0%	2260
JI_STM_0_1.93	3	streamline	150	80	60	0%	2260
JI_TRA_0_1.93	3	trapezoid	150	80	60	0%	2260
JI_REC_0_1.93	3	rectangle	150	80	60	0%	2260
JI_REC_0.55_1.93	3	rectangle	150	80	60	4%	2260
JI_REC_0.55_0	3	rectangle	150	80	60	4%	0
COL_STD_0_1.93	3	no hole	–	–	–	0%	2260

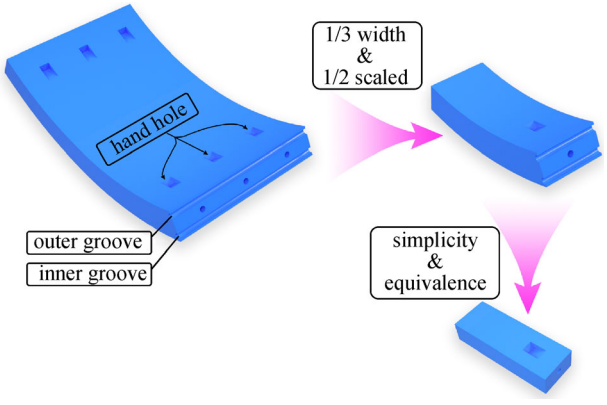

Fig. 1 Simplicity and equivalence of the segment joints

uniaxial loading condition. The detailed joint geometry can be found in Table 1. Figure 2 summarizes the layout and reinforcement details of the RC/MSSF segment joints with inclined rectangle hand hole(JI_REC_0_1.93, JI_REC_0.55_1.93, and JI_REC_0.55_0). The layout and reinforcement details of the other segment joints have been presented in Supplymentary Information(Figs. S1–S5).

2.2 Construction and material properties

The tested reinforced/fiber-reinforced concrete joints were fabricated in a precast plant in Shanghai. After the fresh concrete was poured into the mold, the joint was subsequently vibrated with external vibrators. After compaction and plaster, plastic sheets were placed on the entire mold to reduce steam and moisture losses. After 24 h casting, the joint was taken out and under natural curing with regular wet cotton blankets for 28 days.

The MSSF in this test were provided by EPC Company, China. The geometric and physical properties of the steel fibers used in this test program are presented in Table 2. The concrete mix proportions and properties used in casting the joints are presented in Table 3. Three different sizes of steel bars were used in this test program: 18 mm deformed steel bars and 10 mm plain round steel bars. The steel bar properties used in this test are presented in Table 4. Material tests were carried out for the concrete and the reinforcing steel bar to obtain the material properties. The compressive strength of the concrete mixture was determined from three 150 mm × 150 mm × 150 mm cubic samples according to the CECS 13 [39]. The elastic modulus of the concrete mixture was determined from three 400 mm × 150 mm × 150 mm prism samples according to the CECS 13 [39]. These samples were cast and cured under the same conditions as these joints. Three different sizes of reinforcing steel bars mainly used in the experiments were tested according to the GB/T 28900 [40]. Properties of the concrete and the reinforcing steel bars are presented in Tables 3 and 4, respectively.

2.3 Test setup

The test setup for the 27 reinforced/fiber-reinforced concrete joints is shown in Fig. 1. All these joints were first subjected to monotonic axial loading at a rate of 3 kN/s until the first crack was observed. Then, we employed a displacement control at a rate of 0.2 mm/min until the end of testing. Testing was continued until the resistance of the joints dropped to 30% of the peak axial load. The axial loads were measured by the load cell of the testing machine, while the axial deformation of the joints were measured by 4 LVDTs mounted at each corner of the joints over a gage length of 700 mm. These LVDTs were mounted using 4 angle irons glued to the concrete surface with the hot melt adhesive on the top and a steel clamp on the bottom. Each test set was instrumented with 24 electrical resistance strain gauges (23 strain gauges only in the joints of Str_rec and Ben_rec due to larger hand hole) in order to measure the detailed concrete strain distribution on the surface with hand hole, especially around the hand hole. The overview of the test setup was presented in Fig. 3. Joints were all whitewashed before crack observation. The first hairline crack was observed by naked eye during the loading process. The force and displacement of the actuators were recorded by built-in sensors. The data were logged and recorded by Datataker Data Acquisition System at a frequency of 0.5 Hz.

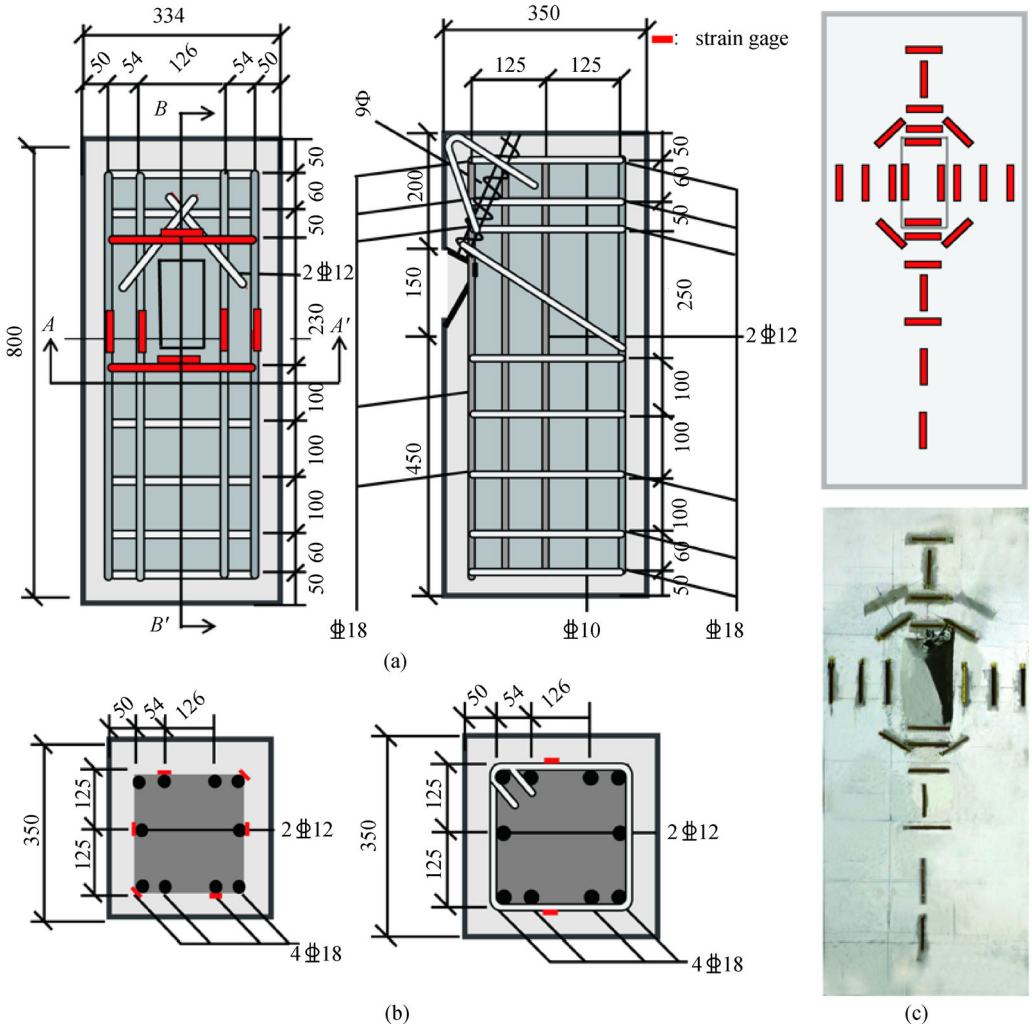

Fig. 2 Geometry and reinforcement details of segment joints. (a) Front view and cross section B-B′; (b) cross section A-A′ and steel strain gauge locations; (c) concrete strain gauge locations. (unit: mm)

Table 2 Structural synthetic fiber properties

item	value
length (mm)	48
modulus of elasticity (GPa)	10
tensile strength (MPa)	640
equivalent diameter (mm)	0.7
density (g/cm^3)	0.91

Table 3 Concrete properties

materials	RC	SFRC
cement	350	350
sand	680	680
coarse aggregate	1159	1159
water	146	146
fly ash	36	36
admixture	3.82	4.32
mineral powder	3	3
fiber dosage	0	0

3 Results and discussions

3.1 Compressive strength

The mean values of the compressive strength of all cubic samples are shown in Table 5. Each value determined by three cubic samples calibrates the compressive strength of corresponding joint. Due to the large amount of concrete and limited number of steel molds are used in this test, these joints have to be manufactured in different batches. The compressive strength of the concrete were required to be as close as possible. The 28-day compressive strength of all the samples is larger than 55 MPa as expected.

Table 4 Steel bar properties

bar	type	usage	diameter (mm)	area (mm^2)	f_y (MPa)	ε_y	E_s (GPa)
steel18	deformed bar	longitudinal reinforcement	18	254.3	465	0.0023	200
steel12	deformed bar	longitudinal reinforcement	12	113.0	478	0.0024	200
steel10	plain bar	transverse reinforcement	10	78.4	423	0.0022	190

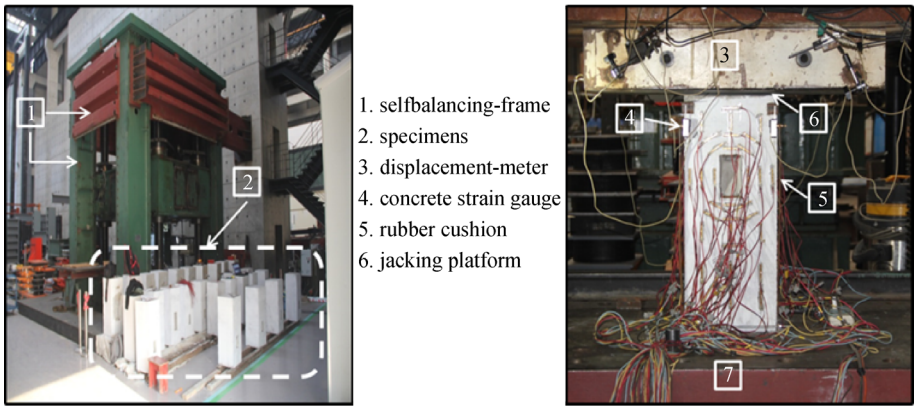

Fig. 3 Overview of the test setup

3.2 General observations and failure modes of the tested specimens

All segment joints specimens were tested until failure. The general behavior of the tested specimens as well as the definition of several parameters used in determining the overall behavior of the segment joint is presented in Fig. 4(a) which is the only one obvious peak point. The behavior presented in Fig. 4(b) is frequently occurring only in the segment joints with straight bolt hole which may be caused by damage effect of the large hand hole and low confinement pressure provided by the transverse stirrups. All these parameters are calculated and summarized in Table 6.

The loads, P_{fcr}, P_{yi}, P_{fp}, and P_{max} are the initial cracking load at the first visible structural micro-crack, the yield load of the segment joints, the axial load of the segment joints at the first peak, the maximum axial load of the segment joints, respectively. The deformation, δ_{yi}, δ_{fp}, δ_{max} are corresponded to the loads P_{yi}, P_{fp}, and P_{max}. f_c is defined as concrete compression strength. The δ_{yi} corresponds to the intersection point between the horizontal line drawn from the PPeak1 and the straight line passes the origin and the point representing the 0.75 times of the P_{fp} [41] as shown in Fig. 4.

Classic compression failures and local failures around the hand hole were observed in combination in this test, except for the specimens without hand holes. Results acquired from the test are mainly listed in Table 6. Figure 5 shows the ultimate failure situation of the specimens. Classic compression failure characteristics appeared on the specimens without the hand hole. When the load approached approximately 42% of the ultimate load, initial minor cracks were observed at both ends of the specimen. With load increasing, large longitudinal penetrating cracks approximately paralleled to the loading direction formed on the specimen before the concrete was finally crushed. For those specimens with hand holes, a kind of combination of classic compression failure characteristics and local failure characteristics appeared. Except for the longitudinal penetrating cracks, a \ /-type crack pattern appeared on the specimens. The formation process of the \ /-type crack pattern is presented in Fig. 6(a). According to the

Table 5 Compressive strength of the concrete

joint	average compressive strength (MPa)	variance (MPa)
JS_REC_0_1.93	59.99	0.703
JB_REC_0_1.93	59.98	0.703
JI_STM_0_1.93	60.29	0.127
JI_TRA_0_1.93	60.33	0.167
JI_REC_0_1.93	59.67	0.104
JI_REC_0.55_1.93	59.68	0.242
JI_REC_0.55_0	60.08	0.391
COL_STD_0_1.93	60.12	0.000

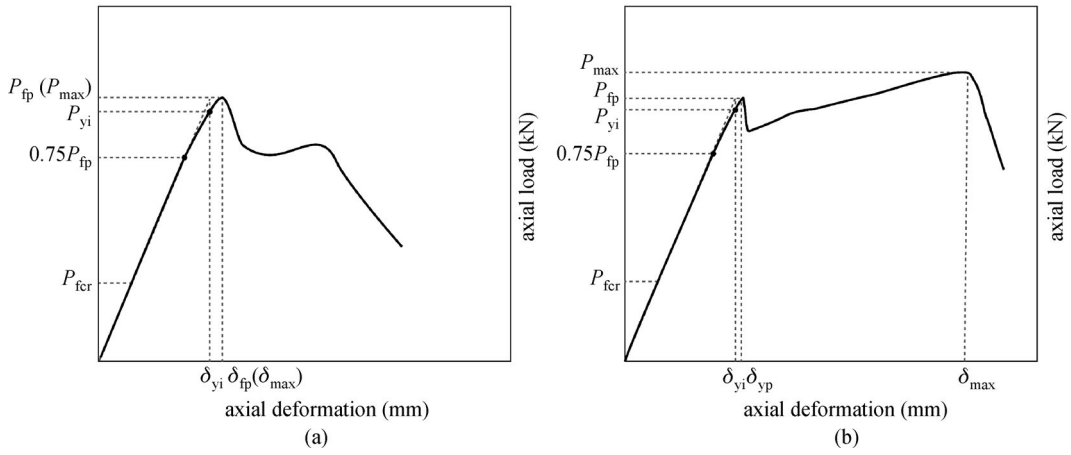

Fig. 4 General behavior of the tested segment joints

experimental observation, the first crack was always appeared as tensile crack near the upper limb of the hand hole. The initial cracking load level of all specimens was recorded in Table 1 as P_{fcr}. As the load increased, a great number of cracks were developed on the specimen. Cracks were mostly distributed around the hand hole and at the both ends of the specimen. With the load further increased, the extension and connection of these cracks gradually leaded to the formation of the \ /-type crack pattern. When the load approached 80%–90% of the ultimate load or approached near the first peak load, the cover of ordinary reinforced concrete specimens began to spall and then detached from the core concrete. However, cover spalling of SFRC specimens was not extensive and was well controlled by MSSF. Detachment of the cover concrete was not occurred even at the ultimate load which is presented in Fig. 6(b).

3.3 Load-deformation relationships

Attention has been barely paid to the influence of the hand hole on the structural behavior of the segment joint in the past research. It was observed that the size and shape of the hand hole has varying degrees of damage on the joint. It is well known that MSSF have beneficial effects on concrete cracking. Moreover, it was also observed that MSSF increase the ultimate capacity and structural reliability of the joint. The load-deflection curves of all testing specimens are presented in Fig. 7.

3.3.1 Influences of the hand hole

It was observed that the size of the hand hole has great affection on the ultimate capacity of the joint, while the shape has much less affection compared to the former. Figure 8 shows the response of the joints with the rectangle hand hole varying size. The other conditions, such as the compressive strength of the concrete as well as the configuration of the transverse reinforcement are quite similar to each other. In Fig. 8, increasing the size of the hand hole from 80 mm×150 mm×60 mm (JI_REC_0_1.93) to 80 mm×250 mm×170 mm (JS_REC_0_1.93) resulted in decreased ultimate capacity by 22.5% and decreased yield deformation by 37.7%. Similar results can be also concluded from Fig. 8, increasing the size of the hand hole from 80 mm×150 mm×60 mm (JI_REC_0_1.93) to 80 mm×200 mm×130 mm (JB_REC_0_1.93) lead to decreased ultimate capacity by 11.5% and decreased yield deformation by 29.6%. Figure 9 shows the response of the joints with the same size hand hole varying in shape. Observed from Fig. 9, shape (streamline, rectangle, and trapezoid) of the hand hole showed much less affection on the ultimate capacity of the joint. Compared to the joints with the rectangle shape hand hole and the trapezoid shape hand hole, the joints with streamline hand hole has an increasing in ultimate capacity by 3.3% and 2.9% in accordance. However, the joints with the streamline shape hand hole have a better deformability than the other two shapes. Compared to the other two shapes, the yield deformation of the streamline shape has an increasing by 31.6% and 15.7%. Unlike the size factor, the influences on the structural behavior of the joints caused by shape mainly focused on the deformability.

3.3.2 Influences of the MSSF

The experiment results in this study showed that the MSSF could improve not only the ultimate capacity of the joints, but also the deformability. This enhancement in the structural behavior of the joints brought by MSSF could make up the damage caused by the hand hole to a certain extent. Since no present formula can be used to calculate the theoretical design ultimate capacity of the joint, the theoretical design ultimate capacity of the concrete

Table 6 Summary of test results

joint	f_c (MPa)	P_{fcr} (kN)	P_{yi} (kN)	P_{fp} (kN)	P_{max} (kN)	$\frac{P_{fcr}}{P_{max}}$	$\frac{P_{yi}}{P_{fp}}$	δ_{yi} (mm)	δ_{fp} (mm)	δ_{max} (mm)	$\frac{\delta_{yi}}{\delta_{fp}}$
JS_REC_0_1.93_A	59.19	700	2460	2560	2657	0.263	0.961	0.354	0.376	0.376	0.941
JS_REC_0_1.93_B	60.52	800	2480	2567	3015	0.265	0.966	0.379	0.396	–	0.957
JS_REC_0_1.93_C	60.25	700	2790	2878	2878	0.243	0.969	0.424	0.439	0.439	0.966
JB_REC_0_1.93_A	60.25	1100	3300	3374	3374	0.326	0.978	0.485	0.529	0.529	0.917
JB_REC_0_1.93_B	59.19	1000	2510	2742	3090	0.324	0.915	0.306	0.349	–	0.877
JB_REC_0_1.93_C	60.52	1100	3250	3414	3414	0.322	0.952	0.501	–	–	
JI_TRA_0_1.93_A	60.37	1400	3421	3667	3705	0.378	0.933	0.580	0.655	0.978	0.885
JI_TRA_0_1.93_B	60.37	1300	3320	3482	3482	0.373	0.953	0.538	0.578	0.578	0.931
JI_TRA_0_1.93_C	60.15	1400	3335	3534	3701	0.378	0.944	0.498	0.538	0.714	0.926
JI_STM_0_1.93_A	60.23	1500	3700	3954	3954	0.379	0.936	0.762	0.922	0.922	0.826
JI_STM_0_1.93_B	60.52	1500	3290	3860	3860	0.389	0.852	0.701	0.894	0.894	0.784
JI_STM_0_1.93_C	60.23	1400	3200	3437	3437	0.407	0.931	0.660	0.725	0.725	0.910
JI_REC_0_1.93_A	59.55	1600	3190	3900	3900	0.410	0.818	0.602	0.855	0.855	0.704
JI_REC_0_1.93_B	59.73	1500	3650	3751	3751	0.400	0.973	0.665	0.687	0.687	0.968
JI_REC_0_1.93_C	59.73	1200	2835	3380	3380	0.385	0.839	0.568	0.695	0.695	0.817
JI_REC_0.55_1.93_A	59.57	1900	4110	4172	4172	0.455	0.985	0.749	0.753	0.753	0.995
JI_REC_0.55_1.93_B	59.1	1900	3650	3681	4107	0.463	0.992	0.730	0.738	1.841	0.989
JI_REC_0.55_1.93_C	60.37	1600	4105	4213	4213	0.404	0.974	0.792	0.904	0.904	0.876
JI_REC_0.55_0_A	60.62	1300	3060	3189	3189	0.408	0.960	0.512	0.607	0.607	0.843
JI_REC_0.55_0_B	60.18	1300	3222	3226	3226	0.403	0.999	0.522	0.523	0.523	0.998
JI_REC_0.55_0_C	59.45	1300	2655	2975	2975	0.437	0.892	0.434	0.533	0.533	0.814
COL_STD_0_1.93_A	60.12	1700	3950	4109	4109	0.414	0.961	0.876	0.933	0.933	0.939
COL_STD_0_1.93_B	60.12	1800	3708	4219	4219	0.427	0.879	0.881	1.454	1.454	0.606
COL_STD_0_1.93_C	60.12	1900	3678	4117	4117	0.462	0.893	0.790	1.715	1.715	0.461

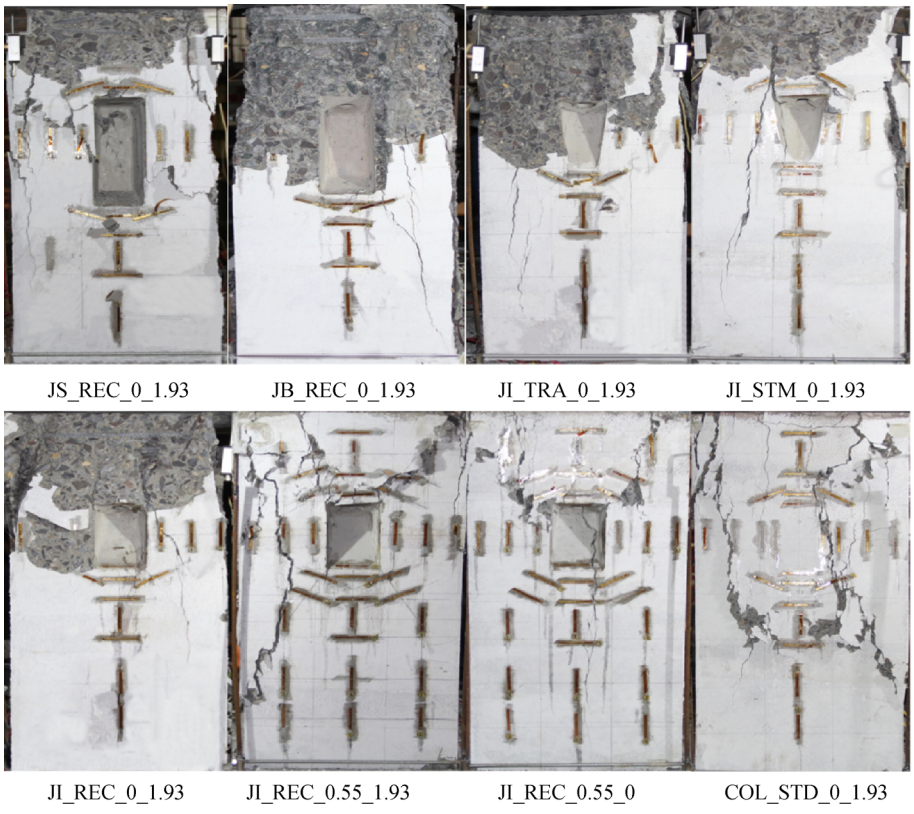

Fig. 5 Ultimate failure mode of test specimens

reinforced column with the same cross section area was used as an approximate theoretical value to evaluate the enhancement brought by MSSF. This approximate theoretical value is calculated according to Chinese National Code (GB50010-2010) [42]. The theoretical design ultimate capacity, N, was determined as follow:

$$N \leqslant 0.9\varphi(f_c A + f_y' A_s')$$

Figure 7 shows the load-deformation relationship of the joints with/without MSSF. The theoretical design ultimate capacity is marked by the horizontal dotted line. By adding MSSF in the joints, the ultimate capacity and yield deformation in Fig. 10 increased by 8.2% and 8% compared to the joints without MSSF. Besides, the structural behavior of the joints without MSSF is observed to be more fluctuant than those joints with MSSF. Similar situations also appeared in other joints indicating that MSSF is beneficial to reducing the variability among specimens and improving structural reliability of the joints.

3.4 Concrete strain and steel strain

Two strain gauges were glued around the hand hole to measure the concrete surface strain. Meanwhile, two strain gauges were also glued to the nearest longitudinal and transverse steels to measure the steel strain. Measured strain values showed that there exists a serious stress concentration near the hand hole. Besides, the degree of the stress concentration varies with different sizes of hand holes. Figure 11 shows the measured tensile and compressive concrete strain of the joints with different sizes of rectangle hand holes and the joints without hand hole. In Fig. 11(a), the tendency of these load-strain curves could be divided into two stages by an obvious yield point. Before the yield point, the load-strain curve is approximately to a straight line. Since then, the curve appears to be nonlinear because of the unstable crack development. The tensile strain at the yield point in this test is around 250, which may only be associated with properties of the concrete. Compared with the COL_STD_0_1.93 specimens, the tensile strain of the joints with the hand hole has an obvious magnification effect. The specific value between the strain of other specimen and the strain of COL_STD_0_1.93 specimen is defined as magnification coefficient, which is recorded in Table 1. The magnification coefficient of the tensile strain between the JS_REC_0_1.93 specimen and COL_STD_0_1.93 specimen at the load of 1500 KN is 3.32, while the coefficient between the Inc_rec1 specimen and the COL_STD_0_1.93 specimen is 1.63. With larger hand hole, the magnification

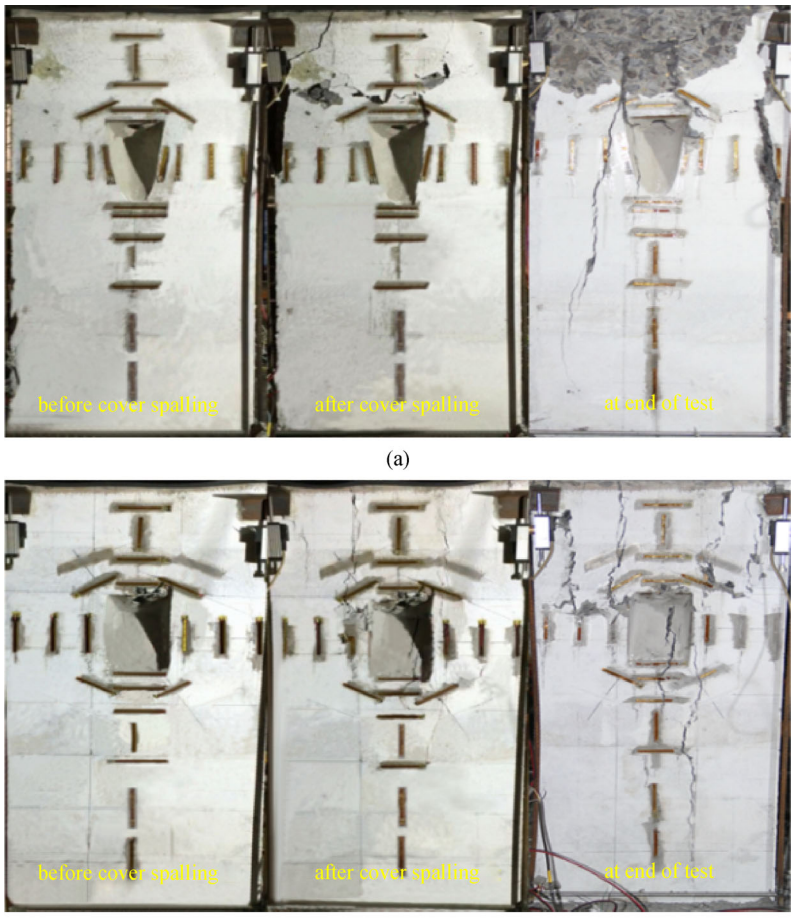

Fig. 6 Failure process of representative joints: (a) RC joint (b) MSSF joint

coefficient is also larger indicating that the stress concentration effect is more significant. By adding the MSSF, the tensile strain magnification coefficient was reduced from 1.63 to 1.42 indicating that MSSF is beneficial to improving the concrete cracking resistance. Similar results were also observed in the compressive strain values. However, the compressive strain magnification effect is not as obvious as the tensile strain.

Figure 12 shows the measured steel strain and concrete strain of the JI_REC_0_1.93A specimen. In Fig. 12(a), the compressive concrete strain is nearly consistent with the corresponding longitudinal steel strain. However, the tensile concrete strain was much larger than the transverse steel strain indicating that the transverse steel has no obvious help in preventing concrete cracking around the hand hole (Fig. 12(b)).

3.5 Joint toughness

The toughness (J) of these joints were calculated by estimating the area under the load-deformation curves at the yield points. It was observed that the JI_REC_0.55_1.93 joint exhibited much higher average toughness at the yield points compared to the other joints (Table 2). This can be attributed to the fact that the yield load and yield deformation of the JI_REC_0_1.93 joint is larger than the other joints. Comparing JI_REC_0.55_1.93 joint with JI_REC_0_1.93 joint, the average toughness increased from 1274.3 to 1501.8 which can be attributed to the application of MSSF. Comparing JI_REC_0_1.93 joint with JS_REC_0_1.93 joint and JB_REC_0_1.93 joint without MSSF, the toughness decreased with the increasing in the size of the hand hole. The toughness of JS_REC_0_1.93 joint and JB_REC_0_1.93 joint was only 39.2% and 67.7% of the JI_REC_0_1.93 joint. Among three shape of the hand hole, the streamline shape hand hole showed the largest toughness of 1341.7 indicating that the joint with streamline shape hand hole could provide better energy absorption ability before failure.

4 Conclusions

This paper presented experimental studies of Reinforced concrete (RC) and MSSF joints varied in the size and shape of the hand hole. The experiments was conducted under

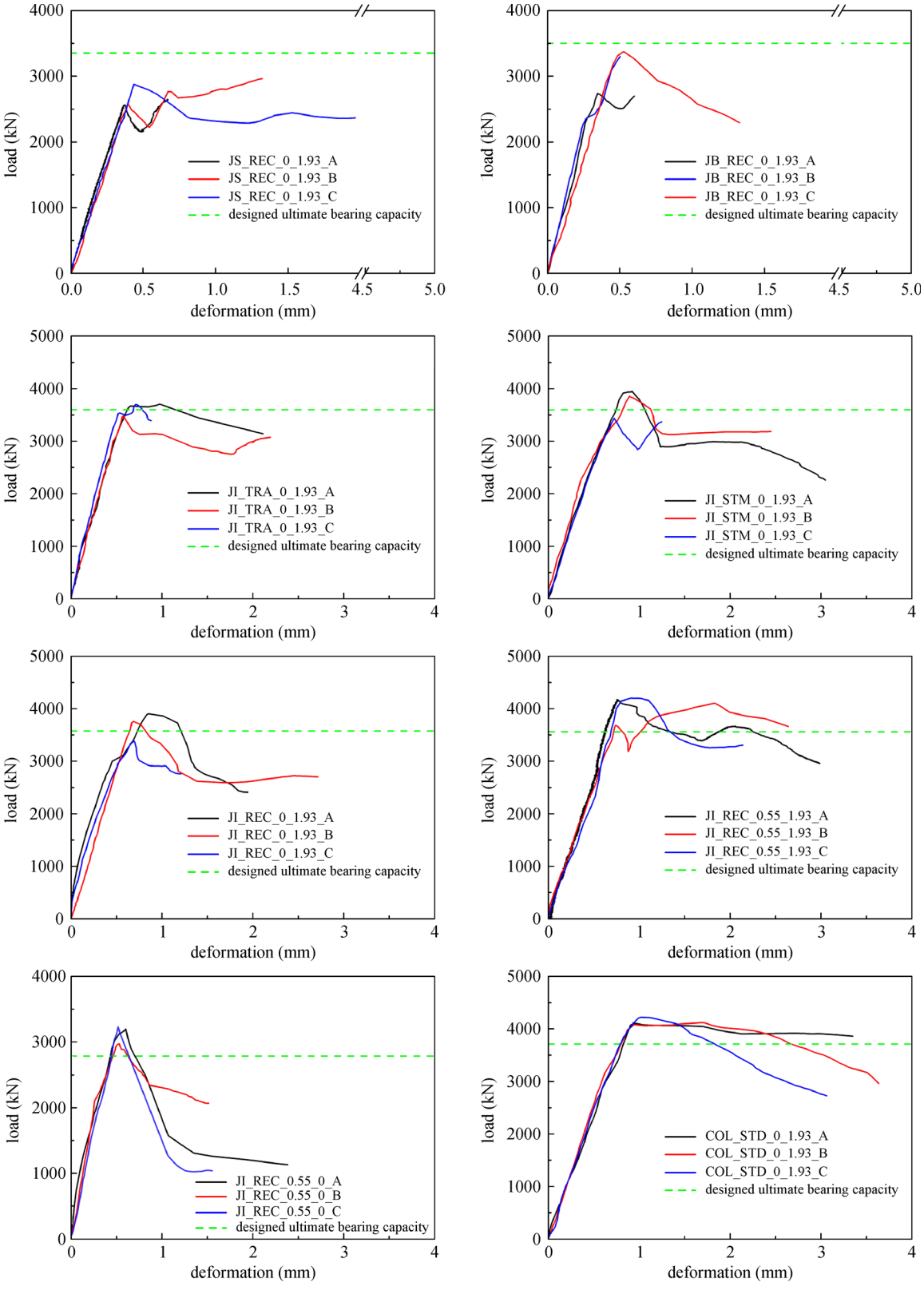

Fig. 7 Load-deformation relationship of all specimens

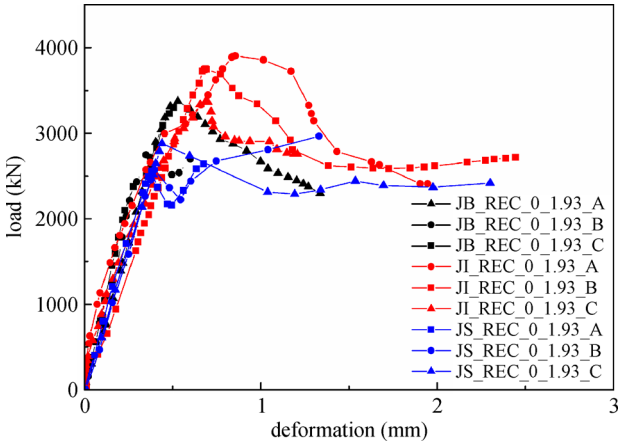

Fig. 8 Influences of hand holes with different sizes on segment joints

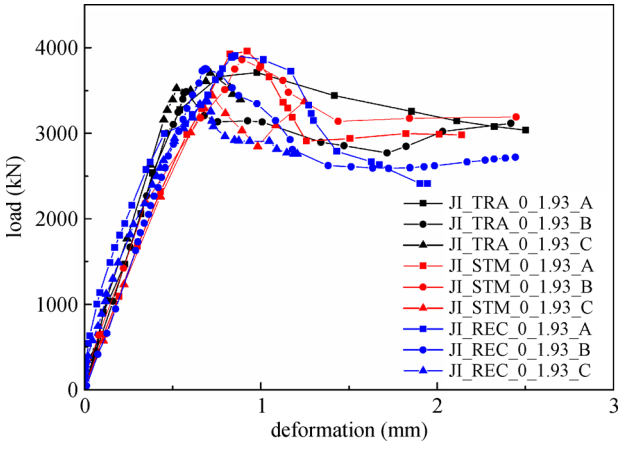

Fig. 9 Influences of hand holes with different shapes on segment joints

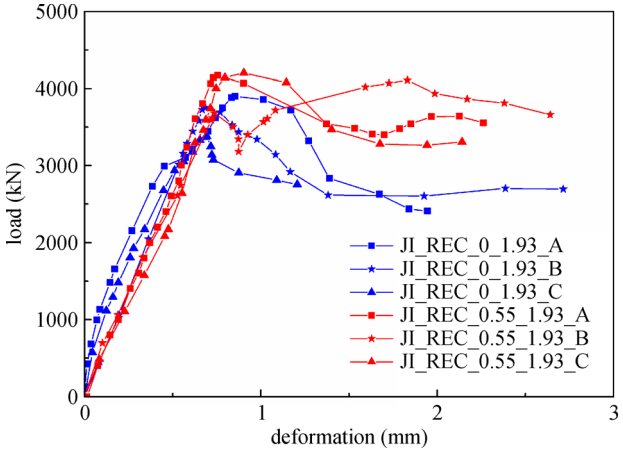

Fig. 10 Influence of MSSF on segment joints

monotonic axial loading aimed to simulate the ultra-high axial force acted on the joints under ultra-high water pressure. The specimens were also simplified based on

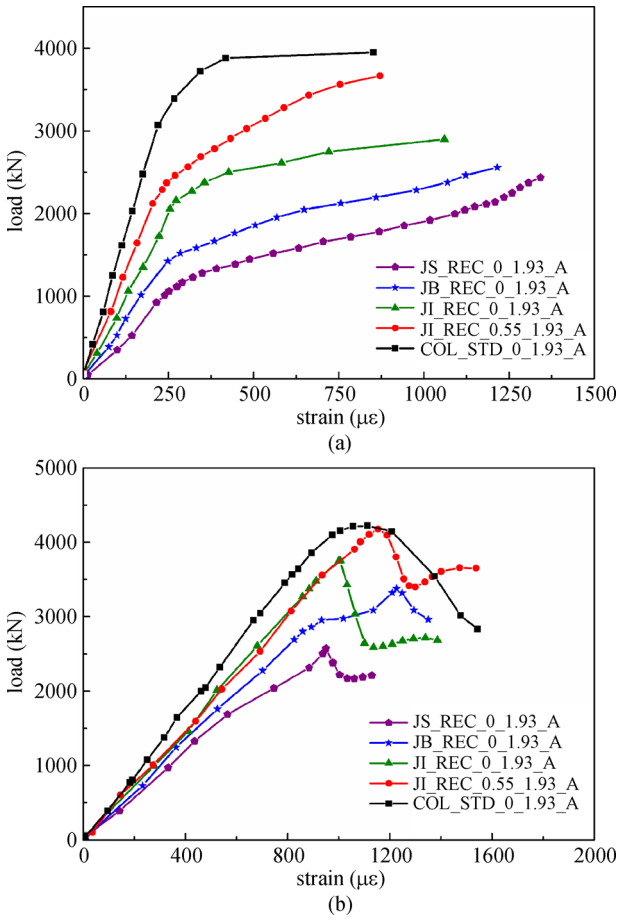

Fig. 11 Tensile and compressive concrete strain of segment joints around the hand hole: (a) tensile strain; (b) compressive strain

existing engineering projects with the aim to study the influence on the structural behavior caused by the hand hole. The findings are summarized as follows:

1) Under ultra-high axial force, the hand hole becomes the critical position of the segment joint. The first structural micro-crack on the concrete surface always tends to appear on the tensile area of the hand hole.

2) Under ultra-high axial force, the failure mode is a combination of global compression failure and local failure. A \ / type crack pattern is always observed before the final failure of the specimens.

3) The application of MSSF improves the initial cracking load of the concrete by restricting the tensile strain around the hand hole. The MSSF joints showed remarked enhancement in the cracking resistance. Furthermore, the MSSF helps to control the premature spalling of the unconfined cover concrete.

4) The MSSF joints exhibit higher ultimate capacity than the RC joints leading to higher reliability in structural design. The application of MSSF in segment joints could increase the ultimate capacity by 8.2%.

5) There exists an obvious stress concentration effect around the hand hole. The tensile strain and compressive

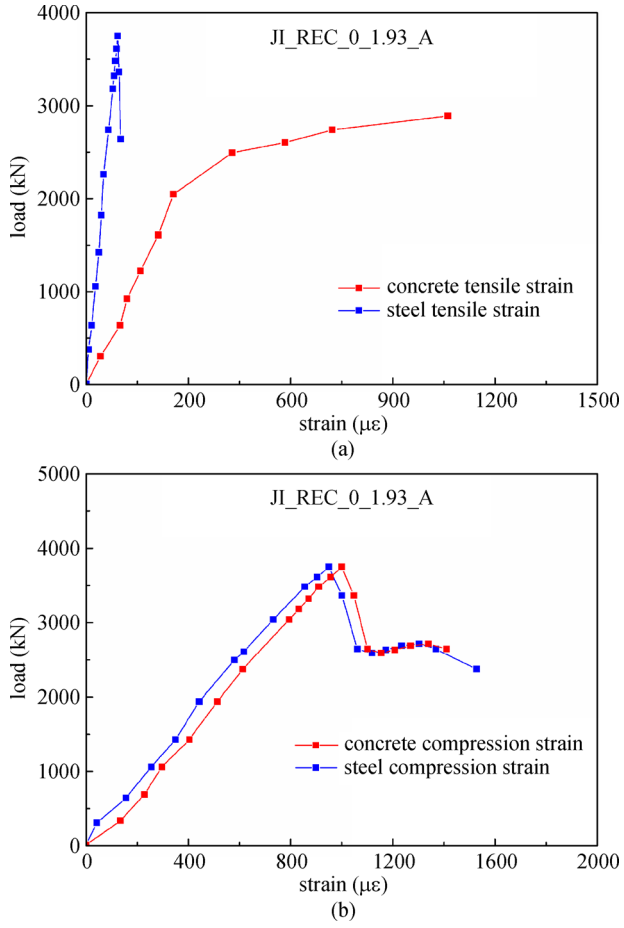

Fig. 12 Tensile and compressive steel strain of segment joints around the hand hole: (a) tensile strain; (b) compressive strain

strain around the hand hole are magnified in varying degrees. The application of MSSF is beneficial to relieve the stress concentration by restricting the tensile strain.

6) The size of the hand hole obviously influences not only the ultimate capacity of the joint, but also the deformability of the joint. The structural performance deteriorates with increasing hand hole size. However, the shape of the hand hole only influences the deformability of the joint. The streamline shape exhibits a better structural performance compared with the other two shapes.

7) The joints with smaller hand hole and MSSF exhibit higher toughness than other joints. Therefore, the joints with smaller hand hole and MSSF show remarked energy absorption ability before failure.

In the future, we intend to carry out a sensitivity analysis as suggested in Refs. [43,44] in order to quantify the key input parameters governing the failure and load carrying capacity. Furthermore, we aim to carry out numerical simulations as done in Refs. [45,46] in order to gain a better understanding of the failure mechanisms. This allows also for parameter studies which reduces costs and time related to experiments.

Acknowledgements This work is funded by the National Basic Research Program, 973 Program (No. 2015CB057804), which is gratefully acknowledged. Special thanks are due to Prof. Bai Yun from Tongji University for his valuable instructions on this work. The assistance from graduate students in Tongji University, Xi Jiang, Likuan Dong, and Ben Cao were essential for the test execution.

References

1. Mashimo H, Ishimura T. Evaluation of the load on shield tunnel

Table 7 Concrete strain magnification coefficient of different segment joints

joint type	JS_REC_0_1.93	JB_REC_0_1.93	JI_REC_0_1.93	JI_REC_0.55_1.93	COL_STD_0_1.93
tensile strain ($\mu\varepsilon$)	236	174	116	101	71
compressive strain ($\mu\varepsilon$)	347	305	281	265	236
magnification coefficient (tensile)	3.32	2.45	1.63	1.42	1
magnification coefficient (compressive)	1.47	1.29	1.19	1.12	1

Table 8 Joint toughness

joint	average toughness	CV
JS_REC_0_1.93	499.7	0.125
JB_REC_0_1.93	863.3	0.067
JI_STM_0_1.93	1341.7	0.092
JI_TRA_0_1.93	1050.3	0.081
JI_REC_0_1.93	1274.3	0.064
JI_REC_0.55_1.93	1501.8	0.070
JI_REC_0.55_0	883.0	0.038
COL_STD_0_1.93	1645.1	0.097

lining in gravel. Tunnelling & Underground Space Technology Incorporating Trenchless Technology Research, 2003, 18(2–3): 233–241
2. Koyama Y. Present status and technology of shield tunneling method in Japan. Tunnelling & Underground Space Technology Incorporating Trenchless Technology Research, 2003, 18(2–3): 145–159
3. Ita W G. Guidelines for the Design of Shield Tunnel Lining. 2000
4. Ding W Q, Peng Y C, Yan Z G, Shen B W, Zhu H H, Wei X X. Full-scale testing and modeling of the mechanical behavior of shield TBM tunnel joints. Structural Engineering and Mechanics, 2013, 45(3): 337–354
5. Ding W Q, Yue Z Q, Tham L G, Zhu H H, Lee C F, Hashimoto T. Analysis of shield tunnel. International Journal for Numerical and Analytical Methods in Geomechanics, 2004, 28(1): 57–91
6. Li Z, Soga K, Wang F, Wright P, Tsuno K. Behaviour of cast-iron tunnel segmental joint from the 3D FE analyses and development of a new bolt-spring model. Tunnelling & Underground Space Technology Incorporating Trenchless Technology Research, 2014, 41(1): 176–192
7. Feng K, He C, Fang Y, Jiang Y. Study on the mechanical behavior of lining structure for underwater shield tunnel of high-speed railway. Advances in Structural Engineering, 2013, 16(8): 1381–1399
8. Liu X, Bai Y, Yuan Y, Mang H A. Experimental investigation of the ultimate bearing capacity of continuously jointed segmental tunnel linings. Structure and Infrastructure Engineering, 2016, 12(10): 1364–1379
9. Budarapu P R, Gracie R, Bordas S P A, Rabczuk T. An adaptive multiscale method for quasi-static crack growth. Computational Mechanics, 2014, 53(6): 1129–1148
10. Budarapu P R, Gracie R, Yang S W, Zhuang X, Rabczuk T. Efficient coarse graining in multiscale modeling of fracture. Theoretical and Applied Fracture Mechanics, 2014, 69(2): 126–143
11. Talebi H, Silani M, Bordas S P A, Kerfriden P, Rabczuk T. A computational library for multiscale modeling of material failure. Computational Mechanics, 2014, 53(5): 1047–1071
12. Talebi H, Silani M, Rabczuk T. Concurrent multiscale modeling of three dimensional crack and dislocation propagation. Advances in Engineering Software, 2015, 80: 82–92
13. Rabczuk T, Zi G, Bordas S, Nguyen-Xuan H. A geometrically non-linear three-dimensional cohesive crack method for reinforced concrete structures. Engineering Fracture Mechanics, 2008, 75(16): 4740–4758
14. Chau-Dinh T, Zi G, Lee P S, Rabczuk T, Song J H. Phantom-node method for shell models with arbitrary cracks. Computers & Structures, 2012, 92–93(3): 242–256
15. Rabczuk T, Areias P M A, Belytschko T. A meshfree thin shell method for non-linear dynamic fracture. International Journal for Numerical Methods in Engineering, 2007, 72(5): 524–548
16. Nguyen-Thanh N, Valizadeh N, Nguyen M N, Nguyen-Xuan H, Zhuang X, Areias P, Zi G, Bazilevs Y, De Lorenzis L, Rabczuk T. An extended isogeometric thin shell analysis based on Kirchhoff-Love theory. Computer Methods in Applied Mechanics and Engineering, 2015, 284: 265–291
17. Rabczuk T, Gracie R, Song J H, Belytschko T. Immersed particle method for fluid-structure interaction. International Journal for Numerical Methods in Engineering, 2010, 81(1): 48–71
18. Areias P, Reinoso J, Camanho P P, Sá J C D, Rabczuk T. Effective 2D and 3D crack propagation with local mesh refinement and the screened Poisson equation. Engineering Fracture Mechanics, 2017, 189: 339–360
19. Areias P, Rabczuk T. Steiner-point free edge cutting of tetrahedral meshes with applications in fracture. Finite Elements in Analysis and Design, 2017, 132: 27–41
20. Areias P, Msekh M A, Rabczuk T. Damage and fracture algorithm using the screened Poisson equation and local remeshing. Engineering Fracture Mechanics, 2016, 158: 116–143
21. Areias P, Rabczuk T, Camanho P P. Finite strain fracture of 2D problems with injected anisotropic softening elements. Theoretical and Applied Fracture Mechanics, 2014, 72: 50–63
22. Areias P, Rabczuk T, Dias-Da-Costa D. Element-wise fracture algorithm based on rotation of edges. Engineering Fracture Mechanics, 2013, 110(3): 113–137
23. Areias P, Rabczuk T. Finite strain fracture of plates and shells with configurational forces and edge rotations. International Journal for Numerical Methods in Engineering, 2013, 94(12): 1099–1122
24. Nguyen-Xuan H, Liu G R, Bordas S, Natarajan S, Rabczuk T. An adaptive singular ES-FEM for mechanics problems with singular field of arbitrary order. Computer Methods in Applied Mechanics and Engineering, 2013, 253: 252–273
25. Rabczuk T, Zi G, Bordas S, Nguyen-Xuan H. A simple and robust three-dimensional cracking-particle method without enrichment. Computer Methods in Applied Mechanics and Engineering, 2010, 199(37–40): 2437–2455
26. Rabczuk T, Belytschko T. A three-dimensional large deformation meshfree method for arbitrary evolving cracks. Computer Methods in Applied Mechanics and Engineering, 2007, 196(29–30): 2777–2799
27. Rabczuk T, Belytschko T. Cracking particles: A simplified meshfree method for arbitrary evolving cracks. International Journal for Numerical Methods in Engineering, 2004, 61(13): 2316–2343
28. Ghorashi S S, Valizadeh N, Mohammadi S, Rabczuk T. T-spline based XIGA for fracture analysis of orthotropic media. Computers & Structures, 2015, 147: 138–146
29. Nanthakumar S S, Lahmer T, Zhuang X, Zi G, Rabczuk T. Detection of material interfaces using a regularized level set method in piezoelectric structures. Inverse Problems in Science and Engineering, 2015, 24(1): 1–24
30. Rabczuk T, Bordas S, Zi G. On three-dimensional modelling of crack growth using partition of unity methods. Computers & Structures, 2010, 88(23–24): 1391–1411
31. Ren H, Zhuang X, Rabczuk T. Dual-horizon peridynamics: A stable solution to varying horizons. Computer Methods in Applied Mechanics and Engineering, 2017, 318: 762–782
32. Ren H, Zhuang X, Cai Y, Rabczuk T. Dual-horizon peridynamics. International Journal for Numerical Methods in Engineering, 2016, 108(12): 1451–1476
33. Amiri F, Anitescu C, Arroyo M, Bordas S P A, Rabczuk T. XLME interpolants, a seamless bridge between XFEM and enriched meshless methods. Computational Mechanics, 2014, 53(1): 45–57

34. Areias P, Rabczuk T, Msekh M A. Phase-field analysis of finite-strain plates and shells including element subdivision. Computer Methods in Applied Mechanics and Engineering, 2016, 312: 322–350
35. Amiri F, Millán D, Shen Y, Rabczuk T, Arroyo M. Phase-field modeling of fracture in linear thin shells. Theoretical and Applied Fracture Mechanics, 2014, 69(2): 102–109
36. Zhuang X, Huang R, Liang C, Rabczuk T. A coupled thermo-hydro-mechanical model of jointed hard rock for compressed air energy storage. Mathematical Problems in Engineering, 2014, 2014, 179169
37. Kasper T, Edvardsen C, Wittneben G, Neumann D. Lining design for the district heating tunnel in Copenhagen with steel fibre reinforced concrete segments. Tunnelling and Underground Space Technology incorporating Trenchless Technology Research, 2008, 23(5): 574–587
38. Timoshenko S P, Goodier J N. Theory of Elasticity. New York: McGraw-Hill, 1951
39. CECS13. Standard test methods for fiber reinforced concrete. 2009 (in Chinese)
40. GB/T28900. Test methods of steel for reinforcement of concrete. 2012 (in Chinese)
41. Foster S J, Attard M M. Experimental tests on eccentrically loaded high strength concrete columns. ACI Structural Journal, 1997, 94(3): 295–303
42. GB50010. Code for design of concrete structures. 2010 (in Chinese)
43. Vu-Bac N, Lahmer T, Zhuang X, Nguyen-Thoi T, Rabczuk T. A software framework for probabilistic sensitivity analysis for computationally expensive models. Advances in Engineering Software, 2016, 100: 19–31
44. Hamdia K M, Silani M, Zhuang X, He P, Rabczuk T. Stochastic analysis of the fracture toughness of polymeric nanoparticle composites using polynomial chaos expansions. International Journal of Fracture, 2017, 206(2): 215–227
45. Rabczuk T, Belytschko T. Application of particle methods to static fracture of reinforced concrete structures. International Journal of Fracture, 2006, 137(1–4): 19–49
46. Rabczuk T, Akkermann J, Eibl J. A numerical model for reinforced concrete structures. International Journal of Solids and Structures, 2005, 42(5–6): 1327–1354